

Rotational asymmetry of pulsar profiles

J. Dyks¹, G. A. E. Wright², and P. Demorest³

¹*Nicolaus Copernicus Astronomical Center, Toruń, Poland*

²*Astronomy Centre, University of Sussex, Falmer, BN1 9QJ, UK*

³*Department of Astronomy, University of California, Berkeley, CA 94720-3411*

Accepted Received ...; in original form 2008 November 28

ABSTRACT

We analyse the influence of rotation on shapes of pulse profiles of fast-rotating (millisecond) pulsars. Corotation has two opposing effects: 1) the caustic enhancement of the trailing side (TS) by aberration and retardation (AR), which squeezes the emission into a narrower phase interval; 2) the weakening of the TS caused by the asymmetry of curvature radiation about the dipole axis. Analysis of the radii of curvature of electron trajectories in the inertial observer’s frame (IOF) enables these two effects to be considered together. We demonstrate that for dipolar magnetic field lines on the TS there exists a ‘caustic phase’ beyond which no emission can be observed. This phase corresponds to the zero (or minimum) curvature of the IOF trajectories and *maximum* bunching of the emission. The maximum gradient of polarisation angle (PA) in the S-shaped PA curve is also associated with the curvature minimum and occurs at exactly the same phase. The asymmetry of trajectory curvature with respect to the dipole axis affects the curvature emissivity and the efficiency of pair production, suggesting a *minimum* at the caustic phase. Emission over a fixed range of altitudes, as expected in millisecond pulsars, leads to broad leading profiles and sharp peaks with a cutoff phase on the TS. We apply our results to the main pulse of the 5 ms pulsar J1012+5307.

Key words: pulsars: general – pulsars: individual: J1012+5307 – Radiation mechanisms: non-thermal.

1 INTRODUCTION

We analyse two specific issues that are important for the appearance of pulse-averaged profiles of pulsars: 1) the radial extent of a region emitting at a given radio frequency, and 2) the asymmetry about the magnetic axis of the curvature of electrons’ trajectories measured in the observer frame. The influence of both of these factors on profile shape is closely associated with the rotation of the magnetosphere, so they should be most noticeable for rapidly rotating objects such as the millisecond pulsars (MSPs). Unlike normal pulsars, MSPs do not exhibit radius-to-frequency mapping (RFM, see figs. 16 and 17 in Kramer et al. 1999). This might possibly be interpreted as near-surface emission with negligible radial extent (McConnell et al. 1996). However, Dyks, Rudak & Demorest (2009) have shown that at least some components in radio pulse profiles are produced when our sightline cuts through the curvature emission from radially-extended plasma streams. In this stream-cut scenario, the observed location of a component is determined by the frequency-independent moment at which our line of sight crosses the plane of a thin stream. When this happens, the component becomes simultaneously recorded at all frequencies that are emitted at the altitude of the cut. There is

no RFM, because positions of components are fixed by the geometry of the cut.

This interpretation requires that a broad range of radio frequencies is emitted by the stream at a fixed altitude. Such a possibility arises naturally in the stream-cut scenario, because density of plasma in a stream decreases in the transverse direction from the stream axis. Therefore, regardless of the altitude that is considered, a broad range of plasma densities (and plasma frequencies) is available at different transverse distances from the stream axis. It is then possible to have a radially-extended emission region (a stream) which provides a range of plasma frequencies at each altitude (the ‘radius-to-frequency’ mapping is replaced with the ‘stream-diameter-to-frequency’ mapping). Thus, the radially-extended emission at a fixed radio frequency is possible without violating the foundation of the RFM idea, that relates the observed frequency to the local plasma frequency at the emission point.¹

The effect of rotation on a radially-extended source can

¹ Needless to say, even in the stream the density must also decrease with altitude, so the RFM is present, but becomes a second-order effect.

be expected to make intrinsically symmetric pulse profiles appear asymmetric with respect to their centre, changing the phases of their components, their intensities and their widths. In the following section (2) we introduce a simple (small-angle) analytical model to determine the likely observable effects in the profiles of fast-rotating pulsars with emitting regions of finite height. These caustic effects are well studied *numerically* and are routinely employed to interpret high-energy pulse profiles of pulsars (Morini 1983; Smith 1986; Romani & Yadigaroglu 1995; Cheng et al. 2000; Dyks & Rudak 2003). Here, however, we focus on the *analytical* study of the phenomenon, which is feasible for low emission altitudes ($r \lesssim 0.1R_{lc}$) or small distances from the dipole axis. This limitation therefore allows possible applications to the radio profiles as well as to specific gamma-ray peaks, eg. those generated by the trailing caustics of the two-pole caustic model.

The results are used to create artificial but instructive pulsar profiles in Section (3). In Section (4) we analyse the curvature of the particle trajectories and examine the impact of considering curvature radiation on model profiles. Then, in Section (6), we see how far our results can model the main pulse profile of J1012+5307. Finally, conclusions are drawn in Section (7).

2 THE PHASE-DEPENDENT EFFECTS OF ROTATION ON PULSAR PROFILES

2.1 Derivation of caustic coordinates

Our ‘simplest case’ model for an averaged pulse profile is limited to the plane of the rotational equator ($\zeta \simeq 90^\circ$, where ζ is the viewing angle measured from the rotation axis $\vec{\Omega}$), and assumes the orthogonal inclination of dipolar magnetic field ($\alpha \simeq 90^\circ$). The \vec{B} -field in the CF is assumed to have the shape of the static dipole.

The radio-emission region is assumed to have the form of a flaring tube/funnel with negligible thickness. It is radially extended, but limited to a single value of the footprint parameter s and it is symmetric with respect to the $(\vec{\Omega}, \vec{\mu})$ -plane (the fiducial plane).

In the CF the radiation from the radial position \vec{r} is emitted at the angle

$$\theta_b \simeq \frac{3}{2}s \sqrt{\frac{r}{R_{lc}}}. \quad (1)$$

with respect to the dipole axis $\vec{\mu}$, where the footprint parameter $s = \sin \theta / \sin \theta_{lo}$, θ is the angle between \vec{r} and $\vec{\mu}$, $\theta_{lo} \approx (r/R_{lc})^{1/2}$ is the θ -coordinate of the last open field lines at the same radial distance r .

The radiation emitted on the leading side (LS) of the dipole axis is therefore detected at the phase

$$\phi_L \simeq -\frac{3}{2}s \sqrt{\frac{r}{R_{lc}}} - 2\frac{r}{R_{lc}} + \phi_f \quad (2)$$

where the term $2r/R_{lc}$ accounts for the leftward shift caused by AR effects, ie. the aberration (contributing one r/R_{lc}) and the retardation (contributing another r/R_{lc}). The symbol ϕ_f denotes the absolute fiducial phase, determined by the detection of a photon emitted from the center of the

NS exactly at the moment when the dipole axis was in the $\vec{\Omega}$ -observer plane (see Dyks 2008 for details).

The radiation on the trailing side (TS) of the dipole axis is detected at the phase:

$$\phi_T \simeq \frac{3}{2}s \sqrt{\frac{r}{R_{lc}}} - 2\frac{r}{R_{lc}} + \phi_f. \quad (3)$$

The opposing signs of the r -dependent terms in eq. (3) mean that on the TS the AR effects tend to cancel the effect of the curvature of \vec{B} -field lines, leading to specific caustic effects. In fact, for arbitrarily large r it is easily possible for the TS-radiation to arrive/be observed on the *leading* side of the profile (especially if s is small).

Let us consider electrons moving upward along a magnetic field line with parameter s on the TS of the open region. As their altitude increases, their radiation is detected at progressively later phases until, at an altitude of r_{cst} , an increment in height of an electron’s trajectory yields an increase in the linear term in eq. (3) which is greater than that of the square root term. Emission is then detected at the phase ϕ_{cst} , which is ‘the latest-possible detection phase’ for a magnetic fieldline with a given s , because further increase in r does not produce any advance in detection phase. For still larger altitudes, the radiation becomes detected at phases *earlier* than ϕ_{cst} . At phases satisfying $\phi \lesssim \phi_{cst}$ it is therefore possible to observe radiation from particles at two different emission altitudes on the *same* fieldline (because the quadratic eq. (3) for r has two real roots).

For a given s the height r_{cst} and phase ϕ_{cst} can be found by using eq. (3) to solve the equation:

$$\frac{d\phi_T}{dr} = \frac{1}{R_{lc}} \left(\frac{3s}{4} \left[\frac{R_{lc}}{r} \right]^{1/2} - 2 \right) = 0, \quad (4)$$

which gives the magnetospheric location of the optimally caustically-enhanced emission:

$$\frac{r_{cst}}{R_{lc}} \simeq \frac{9}{64}s^2. \quad (5)$$

Then, from eq. (3):

$$\phi_{cst} \simeq \frac{9}{32}s^2 + \phi_f = 16^\circ 11s^2 + \phi_f. \quad (6)$$

Thus, for $\alpha \simeq \zeta \simeq 90^\circ$ no tangent-to- \vec{B} radiation emitted within the open fieldline region ($s \leq 1$) can be detected later than 16° after the fiducial phase, regardless of the emission altitude.

Hereafter the ‘caustic’ coordinates of eq. (5) will be denoted by r_{cst} and $s_{cst} = s_{cst}(r)$, and the ‘caustic enhancement phase’ by ϕ_{cst} .

2.2 Caustic phase compression

To estimate the deforming effects of aberration and retardation on a pulsar’s profile, let us assume that all radiation is emitted between radial distances r_1 and r_2 (where $r_1 < r_2$), and that $\Delta r < R_{lc}$. The radial limits will in general refer to some selected frequency, so strictly we should write $r_{\nu,1}$ and $r_{\nu,2}$, but the index ν will be omitted for simplicity.

From eq. (2) the LS radiation emitted between r_1 and r_2 is therefore spread over the phase range:

$$\Delta\phi_L = \phi_L(r_2) - \phi_L(r_1) \simeq$$

$$\simeq -\frac{3}{2}s \left[\sqrt{\frac{r_2}{R_{lc}}} - \sqrt{\frac{r_1}{R_{lc}}} \right] - 2 \left[\frac{r_2}{R_{lc}} - \frac{r_1}{R_{lc}} \right]. \quad (7)$$

The spreading is amplified by the second bracket of eq. (7), which increases $|\Delta\phi_L|$ with respect to the case with the aberration and retardation ignored.² Similarly, for the equivalent fieldline s on the trailing side we use eq. (3) to give the *net* change in phase:

$$\begin{aligned} \Delta\phi_T &= \phi_T(r_2) - \phi_T(r_1) \simeq \\ &\simeq \frac{3}{2}s \left[\sqrt{\frac{r_2}{R_{lc}}} - \sqrt{\frac{r_1}{R_{lc}}} \right] - 2 \left[\frac{r_2}{R_{lc}} - \frac{r_1}{R_{lc}} \right]. \end{aligned} \quad (8)$$

In contrast to eq. (2), the terms of eq. (3) have opposite signs which makes $|\Delta\phi_T| < |\Delta\phi_L|$ whenever $r_2 > r_1$ and $s \neq 0$. Because of this, the radiation on the TS ‘piles up’ within a narrower phase range than on the LS and becomes intensified.

If we interpret eqs. (7) and (8) as component widths generated by the same fieldline s on the LS and TS respectively, then we may compare them by expanding eqs. (7) and (8) about any emission radius r with $r_2 > r > r_1$, giving

$$\Delta\phi_L \simeq \frac{\Delta r}{R_{lc}} \left(-\frac{3s}{4} \left[\frac{R_{lc}}{r} \right]^{1/2} - 2 \right) + O(\Delta r)^2, \quad (9)$$

for the LS and

$$\Delta\phi_T \simeq \frac{\Delta r}{R_{lc}} \left(\frac{3s}{4} \left[\frac{R_{lc}}{r} \right]^{1/2} - 2 \right) + O(\Delta r)^2, \quad (10)$$

for the TS. Since both $\Delta\phi_L$ and $\Delta\phi_T$ are to first order linear in Δr , the profile asymmetry does not depend on Δr (the measure of the asymmetry is the ratio of fluxes on the TS and LS: $R_F = F_T/F_L = |\Delta\phi_L|/|\Delta\phi_T|$, see eq. 14 below). Thus, assuming the emissivity in the CF is roughly symmetric with respect to the $(\vec{\Omega}, \vec{\mu})$ -plane, one cannot change the relative intensity of the LS and TS by adjusting the emitter’s radial extent Δr .

However, this calculation fails in a direct vicinity of the caustic coordinates. If the r_{cst} corresponding to s lies between r_1 and r_2 then eqs. (8) and (10) do not give the observed TS component width (because ϕ_T in eqs. (10) is not a monotonic function of r when r is close to r_{cst}). In fact eqs. (8) and (10) understate the component width because the phase shifts above and below r_{cst} partly overlap and cancel one another.

Suppose, for a given s on the TS, the radiation below r_{cst} generates a component width ($\Delta\phi_{T1}$) which is at least partly overlaid by the component width ($\Delta\phi_{T2}$) generated above r_{cst} . Then the observed component width $\Delta\phi_T$ will be the larger of $\Delta\phi_{T1}$ and $\Delta\phi_{T2}$ and both must anyway extend to the phase $\phi_{cst}(s)$. To see this in eq. (8) we set $\Delta r_i = r_{cst} - r_i$ ($i = 1, 2$) and expand $\Delta\phi_{T_i}$ about r_{cst} to the second order to give:

$$\begin{aligned} \Delta\phi_{T_i} &\simeq \frac{\Delta r_i}{R_{lc}} \left(\frac{3s}{4} \left[\frac{R_{lc}}{r_{cst}} \right]^{1/2} - 2 \right) + \\ &+ (-1)^i \frac{3}{16} s \left(\frac{R_{lc}}{r_{cst}} \right)^{\frac{3}{2}} \left(\frac{\Delta r_i}{R_{lc}} \right)^2 \end{aligned} \quad (11)$$

² Throughout this paper the phase intervals that correspond to altitude differences are always defined as the upper-altitude phase minus lower-altitude phase. Therefore, $\Delta\phi_L$ is negative.

The first term, by definition (eq. 5), is zero and the remainder has a sign depending on i , giving

$$\Delta\phi_{T_i} \simeq \frac{(-1)^i R_{lc}}{2 r_{cst}} \left(\frac{\Delta r_i}{R_{lc}} \right)^2 \quad (12)$$

This expression is independent of s , except indirectly through Δr_i . Thus the minimum component width is attained at $\Delta r_1 = \Delta r_2 = \frac{r_2 - r_1}{2}$, where the upper and lower phase shifts exactly overlap.

The results of this section are likely to have important implications for understanding MSP profiles because, as mentioned earlier, these pulsars are thought to have deep emission zones (i.e. large $\Delta r/R_{lc}$) and hence caustic effects can be expected at a wide range of phases ϕ_{cst} , creating narrow, bright components on the TS in contrast to the broad dimmer features on the LS. In any pulsar of given period and with fixed r_1 and r_2 , there will be a definable *caustic zone* in its profile where component narrowing and intensification might be expected. Its range is given by

$$(\phi_{cst})_{r=r_1} - (\phi_{cst})_{r=r_2} = 2 \frac{\Delta r}{R_{lc}}, \quad (13)$$

Note this result does not depend on the absolute value of the emission heights, and will be greatest for pulsars with narrow light cylinders.

2.3 Caustic intensity compression

The more strongly a given component is compressed by AR effects, the larger will be the radio flux observed at the maximum of that component. Thus, assuming uniform emissivity, the phase-dependent flux (profile shape) can be estimated as:

$$F(\phi) \propto \frac{\Delta r}{|\Delta\phi(\phi)|}, \quad (14)$$

where $|\Delta\phi(\phi)|$ is a width of a component located at pulse phase ϕ . The quantity $F(\phi)$ represents the flux at the maximum of that component.

Eq. (14) will be satisfactory across most of the profile (always including the LS), so that we are able to use the first-order eqs. (9) and (10). However, eq. (14) cannot be used in a direct vicinity of the caustic coordinates. This is because our model assumes an unphysical radiation pattern (the delta function along the electron velocity). This leads to the infinite value of the phase-resolved flux at $\phi = \phi_{cst}$. The infinity appears because for Δr decreasing down to zero around r_{cst} , the amount of radiation emitted (proportional to Δr), decreases slower than the detection interval $\Delta\phi_T \propto 1/(\Delta r)^2$ (eq. 12).

Although this result is formally correct, it is unphysical because locally the radio waves are emitted into a solid angle of finite width $\Delta\phi_b$. Near the caustic coordinates, that is, for $(r_1, r_2) = (r_{cst} - \Delta r, r_{cst} + \Delta r)$ and $\Delta r \rightarrow 0$, the phase interval $\Delta\phi_T$ becomes negligible in comparison to $\Delta\phi_b$. In such a case, the flux observed at $\phi = \phi_{cst}$ becomes determined by the solid angle of the elementary beam ($\propto \Delta\phi_b^2$), and by Δr . Therefore, the equation 14 is not applicable to the caustic points of the magnetosphere and cannot be used to reliably predict the phase-resolved flux at the caustic phase $[F(\phi = \phi_{cst})]$.

Such caustic effects have already been numerically explored in discussions of the few pulsars found to have high

energy profiles. Eq. (6) is therefore the small-angle equivalent of the phase at which the leading peak of the two-pole caustic or slot-gap model occurs (Dyks & Rudak 2003; Muslimov & Harding 2004). This leading gamma-ray peak is emitted from low altitudes on the trailing side of the polar tube and lags the main radio pulse by $\sim 0.1P$, if the closest pole is viewed at a small impact angle ($\zeta \simeq \alpha$). In this case the phase location of this gamma-ray peak is given by eq. (A4) of the Appendix A for arbitrary dipole inclinations α .

3 THE GENERATION OF ASYMMETRIC PROFILES.

To illustrate the observable effects of AR on a millisecond pulsar we generate artificial profiles for a pulsar assumed to have a period of 5.25 ms^3 and to radiate its emission between heights of $r_1 = 10^6 \text{ cm}$ (approximately the neutron star surface) and $r_2 = 2 \cdot 10^6 \text{ cm}$. Such a pulsar would have $R_{lc} = 25 \cdot 10^6 \text{ cm}$ so that $\frac{r_1}{R_{lc}} = 0.04$ and $\frac{r_2}{R_{lc}} = 0.08$.

In Fig. 1 an intrinsically symmetric 6-component (i.e. 3-cone) emission region is assumed for 2 different sets of s parameters. The first (Fig. 1a) includes an outermost cone on $s = 1$ and has a total width of $55^\circ (= 3\sqrt{\frac{r_2}{R_{lc}}})$, the opening angle of the last closed fieldline at the top of the emission zone). From eqs. (7) and (8) this gives $\Delta\phi_L \simeq 15^\circ$ and $\Delta\phi_T \simeq 3^\circ$, i.e. the leadingmost component is 5 times broader than the trailingmost. The second (Fig. 1b) has narrower cones and the merging of components is more comprehensive on the LS. In both cases, the radial extent causes the LS profiles to assume a ‘boxy’ shape so that even with widely spaced cones the stretched components overlap and false ‘components’ can be created (marked ‘O’ in Fig. 1a). It can also be seen that the stretched components do not always fully merge with each other, so that a single notch can appear (marked ‘N’ in Fig. 1a). Single notches in boxy profiles were described by Cordes (1975) for B1919+21. Simulated polarisation profiles (not shown) demonstrate that the overlap does not lead to any depolarisation, because the overlapping components have similar polarisation angle (and our code assumes they have the same intrinsic polarization degree).

By contrast, the TS components are clearly narrowed and become separated. From eq.(5) it follows that strong caustic effects will be observed on fieldlines with s between 0.53 and 0.75 at phases between 4.5° and 9° . This is precisely the phase range within which the strongest peaks occur (on $s = 0.6$ in case (a) and $s = 0.65$ in case (b)). Note that the height of the strongest components is limited by the phase resolution of our calculation (360 phase bins per period).

Note also that, although the total width of the profile remains unchanged from its CF value ($3\sqrt{\frac{r_2}{R_{lc}}} = 55^\circ$), any central emission on $s = 0$ (on a straight fieldline in the CF) would be spread over 6° between 4.5° and 9° preceding the fiducial phase.

In general, for pulsars with trailing components emitted near r_{cst} the flux at the trailing edge of a profile is then likely

³ This typical MSP period will be used throughout this paper to enable a comparison with the profile of J1012+5307.

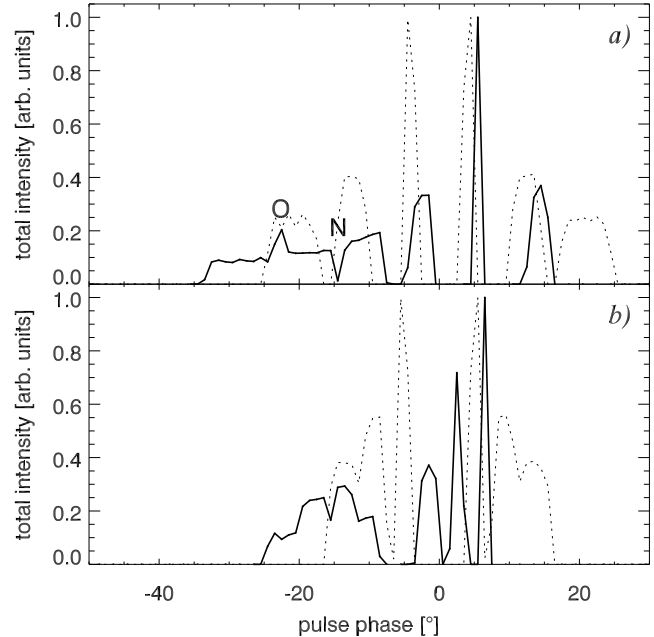


Figure 1. Modelled pulse profiles for the emission region extending radially between 10^6 and $2 \cdot 10^6 \text{ cm}$ in a pulsar with $P = 5.25 \text{ ms}$ and $\alpha = \zeta = 90^\circ$. This implies a *caustic zone* in the profile ranging from 4.5° to 9° . In **a** the radiation is emitted from $s = 0.2, 0.6$, and 1.0 . In **b** $s = 0.25, 0.45$, and 0.65 . The profiles formed without AR effects are shown as dotted lines. In both cases the expected enhancement and narrowing of components occurs in the caustic zone of the TS. The result is for a fictitious emission mechanism with fixed radiative power per each centimeter of electron trajectory in the IOF. Zero on the horizontal axis corresponds to the absolute fiducial phase and the phase resolution is 1° .

to drop more steeply than on the LS. When $\alpha \simeq 90^\circ$ and $s \simeq 1$ on the trailing edge of a pulse, the caustic phase coincides with the trailing edge of a profile if the emission occurs at $r_{\text{cst}}/(10^6 \text{ cm}) = 1, 2, 3.3, 6.7, 67, 670$ for $P = 1.5, 3, 5, 10, 100$, and 1000 ms , respectively. Assuming that the radio emission altitude does not exceed a few tens of R_{NS} we expect steep trailing flanks for profiles of interpulsars with $P < 100 \text{ ms}$.

Sharp features on the trailing side of profiles indeed seem to be a frequent feature among MSPs (J0030+0451, Lommen et al. 2000; J0613-0200, J1022+1001, B1855+09, B1937+21, Kramer et al. 1999; Stairs et al. 1999). In practice it remains difficult to disentangle the components of an MSP and hence to make estimates of r_1 and r_2 . This is mainly because the true position of the fiducial phase within the pulse is unknown and the pulsar’s angle of inclination, which affects our calculation through the generalised forms of eqs. (2) and (3) (see Appendix A), is not easy to estimate. However, as we show below, other consequences of AR may be utilised to give further clues.

3.1 Position angle swing and caustic enhancement

A simple physical description of the caustic pile-up of radiation is that electrons at r_{cst} for a short while move rectilinearly towards the observer in IOF. At $r < r_{\text{cst}}$ their IOF trajectory is bent in the backward/trailing direction,

whereas at $r > r_{\text{cst}}$ it is bent forward because of the domination of the corotation. It is the *inflection point* of the IOF trajectory that is located at $(r_{\text{cst}}, s_{\text{cst}})$ [or $(r_{\text{cst}}, \theta_{\text{cst}})$]. Thus, the region of the caustic pile-up (eq. 5) is simultaneously the region of the zero-curvature of electron trajectory in IOF, as localized by eq. (3) in Dyks (2008). By noting that

$$s \simeq \frac{\theta}{(r/R_{\text{lc}})^{1/2}}, \quad (15)$$

one can rewrite eq. (5) in the forms:

$$\frac{r_{\text{cst}}}{R_{\text{lc}}} \simeq \frac{3}{8}\theta_{\text{cst}}, \quad \text{or:} \quad \theta_{\text{cst}} \simeq \frac{3}{8}s_{\text{cst}}^2. \quad (16)$$

For a *laterally*-extended emitter the zero (or minimum) curvature corresponds to the steepest gradient of the polarization angle swing. The locations of sharp caustic peaks in pulse profiles are then predicted (for a *radially*-extended emitter) to occur at the same phase, ie. $\phi_{\text{cst}} = \phi_{\text{PA}}$. Indeed, eq. (6) can be written as:

$$\phi_{\text{cst}} \simeq \frac{3}{4}\theta_{\text{cst}} + \phi_f \simeq 2\frac{r_{\text{cst}}}{R_{\text{lc}}} + \phi_f \simeq \phi_{\text{PA}}, \quad (17)$$

(cf. eq. 16 in Dyks 2008).

The fact that $\phi_{\text{cst}} = \phi_{\text{PA}}$ does not always mean that caustic enhancement and the PA inflection point will be observed at the same phase in a given object. This is because the relativistically-delayed S-swing is expected for a laterally-extended emitter, whereas the caustic enhancement is for the radially-extended emission, in which case the PA curve does not have to assume the S-shape. Some examples of the PA curves expected for the extreme case of radial extent are shown in Dyks, Harding & Rudak (2004), eg. their fig. 5 is for $\Delta s = 0$ and fig. 7 for $\Delta s \sim 0.05$. Rapid changes of the PA are expected at the caustic peaks and a rather complicated PA curve, cf. the observed optical polarisation data of the Crab pulsar, Słowińska et al. (2009). Moreover, for the specific case of curvature radiation the emissivity vanishes for zero IOF curvature, which can produce a *minimum* of flux at ϕ_{cst} in the averaged pulse profile (see fig. 3 in Blaskiewicz et al. 1991, and the discussion in our Sect. 4.3). We anticipate the case of $\phi_{\text{cst}} = \phi_{\text{PA}}$ to be observable for a slab-shaped emitter with the non-negligible lateral *and* radial extent.

4 CAUSTICS AND EMISSIVITY

4.1 Radius of curvature of electron trajectories in the observer's frame of reference

The corotation increases the curvature of electron trajectories on the LS of the MP, whereas it decreases the curvature on the TS (Ahmadi and Gangadhara 2002; Dyks 2008). The question of how this affects radio emissivity is a complicated one, because it depends on details of the amplification process. One one hand, one can qualitatively argue that the smaller curvature (larger curvature radius) makes the amplification more efficient, because the electrons following less-curved \vec{B} -field interact with narrow beams of radiation for a longer period of time. On the other hand, for the coherent curvature emission from bunches of n charges, the radio emissivity is proportional to the noncoherent curvature emissivity: $F_{\text{coh}} = n^2 F_{\text{cr}}$, where $F_{\text{cr}} \propto \rho_{\text{iof}}^{-2/3}$ is the

noncoherent curvature emissivity of a single electron in the low-frequency limit (Buschauer & Benford 1980), and ρ_{iof} is the radius of curvature of electron trajectory in the inertial observer frame (IOF). This holds at least as long as n is independent of ρ_{iof} .

For the latter mechanism our model for the pulse profile shape becomes:

$$F(\phi) \propto \frac{\rho_{\text{iof}}^{-2/3} \Delta r}{|\Delta\phi(\phi)|}. \quad (18)$$

To use it efficiently, we need a convenient method for estimating ρ_{iof} . The value of ρ_{iof} can be expressed as:

$$\rho_{\text{iof}} \simeq \frac{c^2}{|\vec{a}_{\text{iof}}|}, \quad (19)$$

where \vec{a}_{iof} is the electron acceleration in the IOF. In eq. (19) the electron velocity has been approximated by the speed of light c , and any acceleration parallel to the electron trajectory is thereby neglected.

The IOF acceleration can be expressed as a sum of two vectors:

$$\vec{a}_{\text{iof}} = \vec{a}_B + \vec{a}_\Omega \simeq \frac{c^2}{\rho_B} \hat{\rho}_B + 2\Omega c \hat{e}_\phi, \quad (20)$$

where \vec{a}_B is the CF-acceleration caused by the curvature of magnetic lines and \vec{a}_Ω is the acceleration generated by the corotation (see Dyks 2008 for a simple derivation; note that we still keep the discussion limited to the orthogonal case of $\alpha = \zeta \simeq 90^\circ$). The symbol ρ_B denotes the radius of curvature of \vec{B} -field lines in the CF:

$$\rho_B \simeq \frac{4}{3} \frac{\sqrt{r R_{\text{lc}}}}{s}, \quad (21)$$

$\hat{\rho}_B$ (with a hat) is a unit vector along that radius of curvature, and \hat{e}_ϕ is a unit vector in the direction of the rotational azimuth. In the small-angle approximation, on the leading side in the plane of the rotational equator we have $\hat{\rho}_B \simeq \hat{e}_\phi$. On the trailing side $\hat{\rho}_B \simeq -\hat{e}_\phi$, so that eq. (20) becomes one-dimensional.

Thus, for these specific simple cases we correspondingly have:

$$\rho_{\text{iof,L}} \simeq R_{\text{lc}} \left(\frac{3}{4} \frac{s}{\sqrt{r/R_{\text{lc}}}} + 2 \right)^{-1} = R_{\text{lc}} \left(\frac{R_{\text{lc}}}{\rho_B} + 2 \right)^{-1} \quad (22)$$

(leading side),

$$\rho_{\text{iof,T}} \simeq R_{\text{lc}} \left| \frac{3}{4} \frac{s}{\sqrt{r/R_{\text{lc}}}} - 2 \right|^{-1} = R_{\text{lc}} \left| \frac{R_{\text{lc}}}{\rho_B} - 2 \right|^{-1} \quad (23)$$

(trailing side).

Interestingly, the only difference between ρ_{iof} and the CF-curvature radius of magnetic field lines (eq. 21) is the added number ‘ ± 2 ’ in eqs. (22) and (23). Not surprisingly, apart from the sign issue eq. (23) is the inverse of $d\phi_{\text{T}}/dr$ (eq. 4). This is because the very definition of the curvature radius is $\rho_{\text{iof}} \equiv dl/d\delta$, where dl is an increment of electron trajectory and $d\delta$ is the angular increment corresponding to dl . Because of the small-angle approximation we have $dl \simeq dr$, and because of the near-orthogonality we have $d\delta \simeq d\phi$, ie. a change of the direction tangent to electron trajectory in IOF is equal to the interval of the pulse phase. Thus,

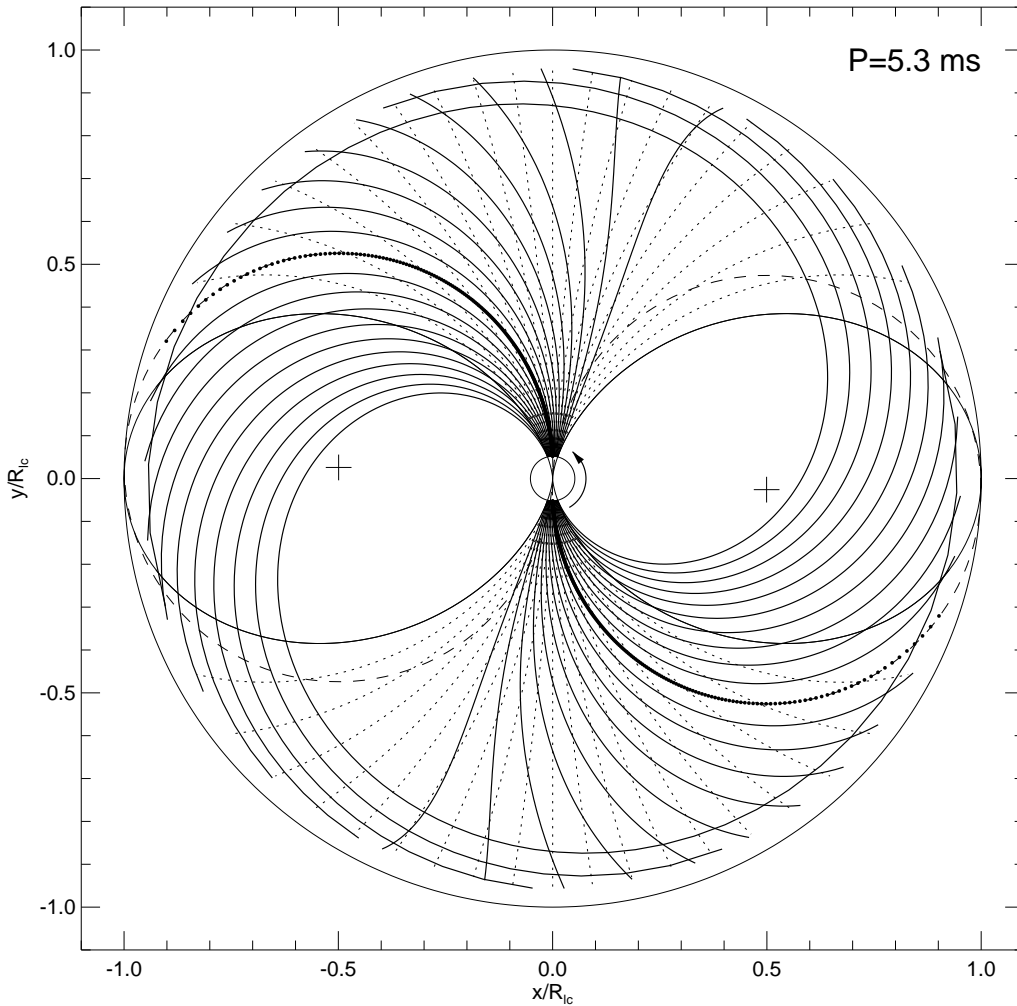


Figure 2. IOF trajectories (thick solid lines) of electrons moving in the equatorial plane of orthogonal pulsar ($\alpha = 90^\circ$). The curves are separated by $\Delta s = 0.1$ and refer to electrons that left the star surface when the dipole axis was vertical in the figure (i.e. the fiducial instant). IOF trajectories for electrons moving along the dipole axis are marked with dots (merging into very thick solid lines) and coincide with the analytical solution (dashed circles of radius $R_{1c}/2$, centered at the crosses on both sides of the star; the centres are located at $x/R_{1c} = \pm 0.5 \mp (0.5R_{NS}/R_{1c})^2$ and $y/R_{1c} = \mp 0.5R_{NS}/R_{1c}$). Electron trajectories in the CF (\vec{B} -field lines) are shown as dotted lines, except for the last open ones, which are thin solid. The outermost circle is the light cylinder. The figure assumes rigid corotation of a static-shape dipole out to $0.95R_{1c}$. The trajectories shown extend from the leading edge to the trailing edge of the open region and have $s = 1, 0.9, 0.8, \dots, 0.1, 0.0, 0.1, \dots, 0.9, 1.0$.

$\rho_{iof} = dl/d\delta \simeq (d\phi/dr)^{-1}$. For $\alpha \simeq 90^\circ$ the ratio of the IOF-curvature radii on the leading and trailing side can thus be conveniently estimated with the help of eqs. (22) and (23) (the model is extended to the nonorthogonal dipole inclinations in Appendix A).

For MSPs with $P \sim$ a few ms, the value of ρ_{iof} on the trailing side of the polar cap surface can be one order of magnitude larger than the equivalent value on the leading side. For $P = 5$ ms and $s = 1$ we have $\rho_{iof,L} = 5 \cdot 10^6$ cm, $\rho_{iof,T} = 2.5 \cdot 10^7$ cm, whereas the dipolar $\rho_B = 8 \cdot 10^6$ cm. The asymmetry of ρ_{iof} about the dipole axis is illustrated in Fig. 2, where particle trajectories in the IOF are shown. It exhibits trajectories from the leading edge to the trailing edge of the open region [there are 21 trajectories that start from each polar cap with footprint parameter s that goes

from 1 on the LS through 0 to 1 on the TS in steps of 0.1]. The gradual increase of curvature radii towards the TS is visible. The dipole axis is marked with merged dots (dark line).

In fact, at fixed r the curvature is completely symmetric about the caustic trajectory, that is, about $s_{cst}(r)$. This can be seen by using eqs. (22) and (23) to transform the basic equations (2) and (3), giving

$$\rho_{iof} = \frac{2r}{|\phi - \phi_{cst}|} \quad (24)$$

Then, if cones are formed with the same IOF curvature they will be symmetric about the caustic phase at any given height r . If a finite range of r is considered the cones will become “blurred” – but nevertheless this cannot lead to the TS

peaks being brought closer together. Fig. 3 shows curvature as a function of altitude for a range of field line parameters (and compares this with our approximate analytical formulae for ρ_{iof} and ρ_B .) This makes clear that our small angle approximation holds well in the region we are interested in.

These results imply that with the knowledge of the curvature radius in the IOF we can transfer the entire discussion of components' widths and intensities into the IOF, without the need to refer to the effects of aberration and retardation. Specifically, eqs. (7) and (8) are equivalent to the natural assumption that the component's width is inversely proportional to the radius of curvature in IOF:

$$\Delta\phi \simeq \frac{\Delta r}{\rho_{\text{iof}}}. \quad (25)$$

This can be immediately proved by comparison of the approximate eqs. (9) and (10) with the formulae for ρ_{iof} (eqs. 22 and 23). *The caustic effects of AR can thus be seen as simply the consequence of an increase of the curvature radius in IOF.*

Our flux model of eq. (18) can then be written

$$F(\phi) \propto \frac{\rho_{\text{iof}}^a \Delta r}{\Delta r / \rho_{\text{iof}}} = \rho_{\text{iof}}^{1-a}. \quad (26)$$

For the non-coherent, low-frequency curvature radiation, the exponent a is equal to $-2/3$, and the equation (26) just reduces to $F(\phi) \propto \rho_{\text{iof}}^{1/3}$, which suggests a weak amplification on the TS. However, as we shall see in the next subsection, more physical considerations are likely to reverse this effect.

As a consequence, the TS of the profile is subject to two potentially competing effects, both dependent on trajectory curvature and hence both having maximum effect around the caustic zone of the profile. On the one hand, the AR bunches the emission of a single fieldline into a narrow phase. On the other, if the coherent radio emissivity decreases with increasing ρ_{iof} (as the model of eq. 18 assumes), this may counteract the caustic amplification.

4.2 Giant pulses at the caustic singularity?

It is also interesting to consider the implications of caustic enhancement for single pulses. The quasi-rectilinear motion of electrons in the caustic regions of magnetosphere makes favourable conditions for coherent amplification, because the interaction between the emitted radiation and particles can last for a longer period of time than in the case of a strongly-curved trajectory. We speculate that this may give rise to 'giant' pulses, whose phase location is determined by eq. 6 (see Appendix A for the non-orthogonal version). At the same time, however, the reduced curvature decreases the emissivity and frequency of the curvature radiation. To overbalance this effect, the efficiency of the amplification process would have to grow with decreasing curvature sufficiently quickly. The energy of electrons has also to be larger for the curvature radiation to extend up to the observed band.

4.3 Rotation and the profile flux balance

Eq. (26) enables us to consider the profile asymmetry in more realistic cases, differing from the basic cases of Fig.1 where Δr was held constant across the profiles and only AR effects were taken into account. Let us assume an emission

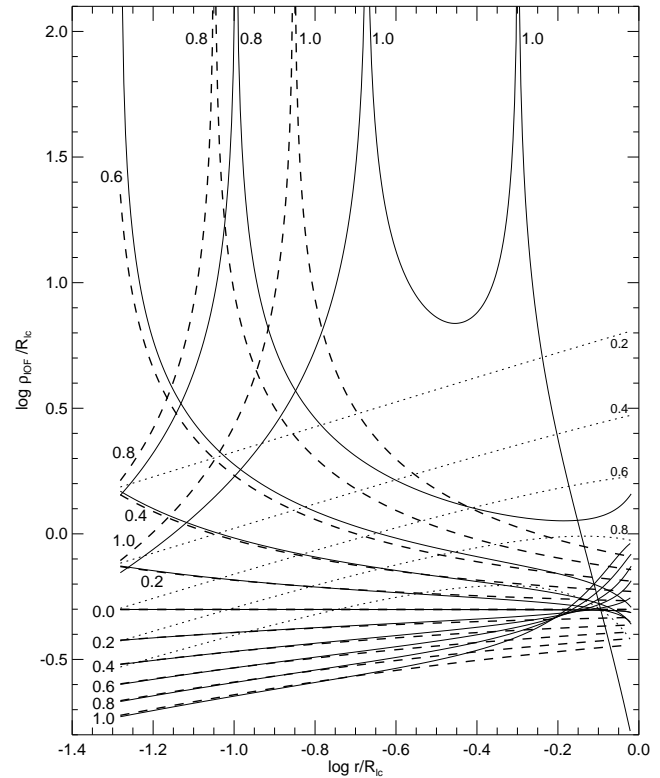


Figure 3. IOF radius of curvature calculated for selected magnetic field lines of a pulsar with $P = 5.25$ ms and $\alpha = 90^\circ$. Solid lines present exact numerical solution and dashed lines are for eqs. (22) and (23). The numbers give the footprint parameter s . Dotted lines (the lowest one for $s = 1$) present the dipolar ρ_B . The horizontal marked with '0.0' is for the dipole axis trajectory ($\rho_{\text{iof}} = R_{\text{lc}}/2$) and separates the lower curves for the LS from the upper lines for TS.

region with the quantity Δr symmetric with respect to the main meridian so that the only asymmetric quantity left is ρ_{iof} . We also allow for a non-negligible range of the footprint parameter Δs associated with a given component because it is easy to model numerically and can be expected in realistic cases. The profile asymmetry is also determined by the value of the exponent a that describes how the intrinsic coherent emissivity depends on ρ_{iof} . In the discussion below we assume $a = -2/3$ for definiteness [non-coherent curvature radiation (CR) in the low-frequency limit].

The effect of non-zero Δs can be modelled by modifying eq. (26) so that

$$F(\phi) \propto \frac{\rho_{\text{iof}}^a \Delta r}{\Delta r / \rho_{\text{iof}} + \frac{3}{2} \sqrt{\frac{r}{R_{\text{lc}}}} \Delta s}. \quad (27)$$

In the case of negligible Δr (ie. for $\Delta r / \rho_{\text{iof}} \ll \frac{3}{2} \sqrt{\frac{r}{R_{\text{lc}}}} \Delta s$ in eq. 27) we have $F \propto \rho_{\text{iof}}^{-2/3}$, ie. the components on TS of the profile are dimmer than those on the LS. This can be seen in Fig. 4a which is calculated for $\Delta r = (r_1, r_2) = (0.04, 0.05) R_{\text{lc}}$ and $\Delta s = \langle s_{\text{min}}, s_{\text{max}} \rangle = \langle 0.9, 1 \rangle$. Fig. 3 in Blaskiewicz et al. (1991) presents a similar case for a region completely filling in the open region [$\Delta s = (0, 1)$].

In Fig. 4b the upper radial distance r_2 is increased to $0.12 R_{\text{lc}}$. This makes the caustic term $\Delta r / \rho_{\text{iof}}$ in eq. (26)

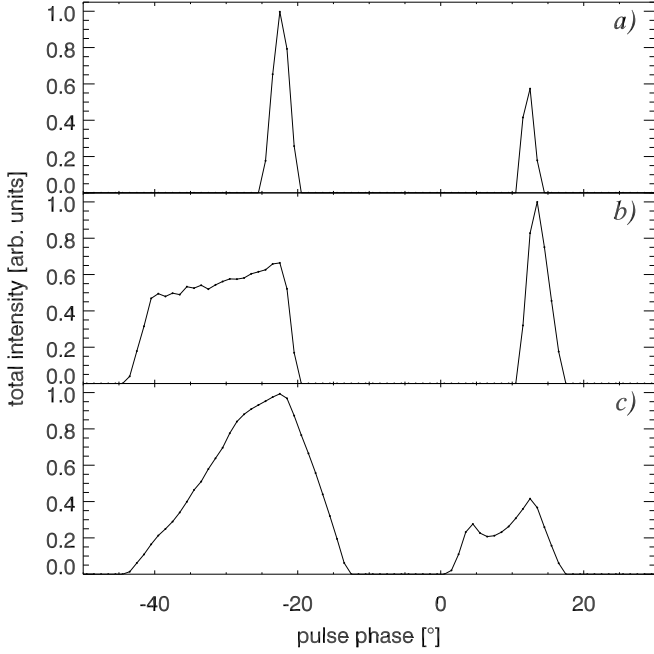


Figure 4. Simulated pulse profiles that show how the rotational asymmetry is affected by changes of $\Delta r = \langle r_1, r_2 \rangle$ and $\Delta s = \langle s_{\min}, s_{\max} \rangle$. In all figures the intrinsic emissivity is proportional to $\rho_{\text{iof}}^{-2/3}$ (non-coherent CR). In **a**) $\Delta s = \langle 0.9, 1 \rangle$, and $\Delta r/R_{\text{lc}} = \langle 0.04, 0.05 \rangle$. In **b**) r_2 is increased to $0.12R_{\text{lc}}$. In **c**) $r_2 = 0.12R_{\text{lc}}$ and $s_{\min} = 0.5$.

more important so that we have $F \propto \rho_{\text{iof}}^{-2/3}$ and the TS component becomes brighter [the component’s ‘brightness’ is understood as the flux at the maximum of the component, not the phase-integrated flux]. For $\Delta s = \langle 0.5, 1 \rangle$ and $r_2 = 0.12R_{\text{lc}}$ (Fig. 4c), the decline of the intrinsic emissivity ($F_{\text{coh}} \propto \rho_{\text{iof}}^{-2/3}$) again dominates over the caustic amplification and the LS component becomes brighter. In addition to the eq. (27) this change of R_F can be understood as follows. The peak flux on the LS is increased because the emission from adjacent s overlaps in phase. On the TS the caustic peaks associated with different s do not occur at the same phase. The larger value of Δs makes the components on the TS wider, but their peak flux is not enhanced considerably. The influence of Δr and Δs on the pulse shape can therefore be summarized in the following two points: 1) the increase of Δr makes the LS components wider and the TS components stronger (larger peak flux, Fig. 4b); 2) the increase of Δs works in just the opposite way: it makes the LS components stronger and the TS components wider (Fig. 4c). When the emissivity is independent of ρ_{iof} ($a = 0$) it is the TS that is *always* brighter, with the flux ratio determined by the relative values of Δr and the intrinsic width $\Delta\phi_{\text{intr}} = (3/2)\sqrt{r/R_{\text{lc}}}\Delta s$.

We therefore conclude that the caustic amplification ($\propto \rho_{\text{iof}}$) makes the TS brighter only if the intrinsic emissivity does not decrease with increasing ρ_{iof} too fast. For the low-frequency CR ($a = -2/3$) the caustic amplification can still dominate over the intrinsic flux decline (as in our Fig. 4b) but this requires special conditions to be fulfilled (small Δs , large Δr).

For large Δr and several emission cones, the above con-

clusions are furthermore complicated by the possible overlap of different components on the LS, which can additionally increase the peak flux on the LS. In the simulated profile of Fig. 1b the two maxima at $\phi = -18^\circ$ and -14° are created by an overlap of emission pattern from three cones. Such an inter-component overlapping is not included in eqs. (26) and (27).

We then find that it is possible (and not unlikely) for the LS to become brighter purely because of the intrinsic dependence of emission mechanism on ρ_{iof} . For $a = -2/3$ the TS can be enhanced only under special circumstances (small Δs , not overlapping components). Narrow and strong trailing components seem to be a frequent phenomenon among MSPs (Kramer et al. 1998; 1999). Moreover, at least some exceptions (with apparently brighter LS) seem to be created by the scattering phenomenon (see eg. fig. 8 in Kramer et al. 1999). This suggests that $-2/3 < a \lesssim 0$, provided we are not biased by unrecognized absorption effects. The results of this section also apply for the models of high-energy emission (even for the polar cap model if applied for pulsars with millisecond periods). In the outer gap and slot gap models, the peaks in the gamma-ray profiles are generated mostly by the caustic effects. They are then formed in the region where the IOF radius of curvature is greatly increased in comparison to the CF value. It is then absolutely necessary to use the IOF curvature radius ρ_{iof} to obtain reliable pulse profiles in the numerical simulations of the CR.

5 PULSARS WITH PHASE-SHIFTED CONES

Gangadhara & Gupta (2001, hereafter GG01), noted that profiles of selected pulsars have outer cones more shifted towards early phase than inner cones. Krzeszowski et al. (2009) find at least a tendency towards this effect in most pulsars in their sample, but they also find some counterexamples (e.g. B1831–04). The forward shift of outer cones was interpreted by GG01 in terms of a lower emission altitude for an inner cone. The detection of such a low-altitude inner cone is delayed by a decrease in the aberration angle and the increased propagation time. This interpretation may be called the ‘cone-altitude effect’. It implies a structured emission region with two rings of different size located at two different altitudes (and with a core emission region near the surface).

Because such a structure has never received a physical explanation it is worth considering whether an alternative scenario exists in which the cones can be actually located at the same altitude, but intrinsically decentered in the CF to produce the forward shift of the cones. A possible natural argument for this is the shift of the pair-production symmetry point towards the TS.

As shown in Fig. 5, for $P = 5.25$ ms and $r = 1.3 \cdot 10^6$ cm, the zero curvature of electron trajectories in the IOF is expected at $s_{\text{cst}} = 0.61$ on the TS of the open region, ie. at a phase $\phi \simeq \phi_{\text{MP1}} + 0.8W_{\text{MP}}$, where W_{MP} is the profile width and ϕ_{MP1} is the location of the first (leadingmost) component.⁴ Conversely, any non-curvature photons emitted by the electrons (moving along the \vec{B} -field line with $s = 0.61$)

⁴ In the case of a rotationally-distorted vacuum dipole the phase is equal to $\phi_{\text{cst}}(R_{\text{NS}}) = \phi_{\text{MP1}} + 0.68W_{\text{MP}}$, because of the boundary of the open region is shifted toward the TS.

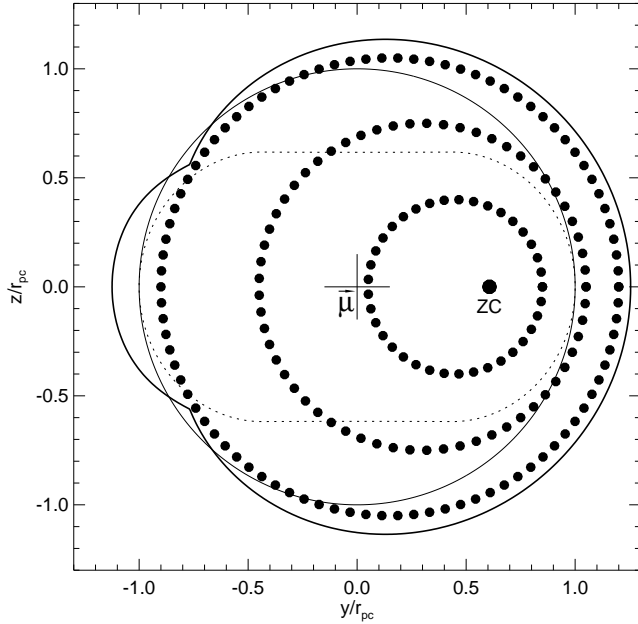


Figure 5. Location of the zero-curvature point (bullet marked ‘ZC’) at the polar cap of a pulsar with $\alpha = 90^\circ$, $P = 5.25$ ms, $R_{\text{NS}} = 1.3 \cdot 10^6$ cm. The curvature of electron trajectories in IOF (thereby the curvature radiation) vanishes at the point where $s = 0.61$. Curved CF trajectories of non-curvature photons that are emitted there coincide with the local \vec{B} -field line in the CF. Thick solid and dotted lines mark the polar cap edge for the retarded and static-shape dipoles. Thin solid circle marks the standard circular polar cap (formally for $\alpha = 0^\circ$). The decentered circles of dots show possible locations of emission cones affected by the ZC point.

propagate in the CF along a *curved* path locally coincident with this \vec{B} -field line and are least likely to participate in any pair-creation cascade (see fig. 7 in Dyks & Rudak 2002). The point of zero IOF curvature is therefore also the location of vanishing (or minimum) pair production. The density distribution of the created e_{\pm} -pairs is then expected to be symmetrical around the ZC point located clearly on the TS of the open region. The same symmetry (centered at the zero-curvature coordinates) can be imposed on the accelerating electric field if it is strongly screened by the pairs.

On the other hand, the general geometry of the open region implies the dipole-centered symmetry. If the outer boundary $s = 1$ has indeed the same electric potential everywhere, the (unscreened) electric field should roughly follow the symmetry of the open dipolar fieldlines (which are centered on the dipole axis, not at the lowest-curvature IOF-trajectory). It is therefore conceivable that any conal emission structures within the open region will be affected by both symmetries and may assume the ‘intermediate-case’ geometry shown in Fig. 5. *This effect can mimic the cone-altitude effect even if all the cones originate at the same altitude.*

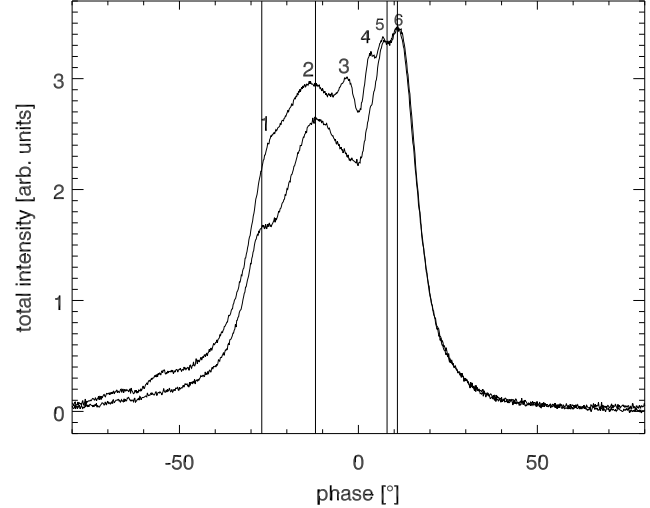


Figure 6. The main pulse of J1012+5307. Radial extent of the radio emission implies different widths of components on the leading and trailing side of the MP. The two pairs of vertical lines present the components’ widths expected for low-altitude emission (between $r_1 = 10^6$ and $r_2 = 2.3 \cdot 10^6$ cm) from the last open field lines ($s = 1$).

6 APPLICATION TO THE MAIN PULSE OF J1012+5307

6.1 Component widths

Fig. 6 presents the main pulse (MP) of a 5.26 ms pulsar J1012+5307 observed at 0.82 GHz (top) and 1.4 MHz (bottom) with the Green Bank Telescope. The bandwidths were 64 MHz at both frequencies and the total integration time of ~ 15 hours spanned the period between July 2004 and March 2007. This pulsar was chosen because it exhibits an interpulse (not shown), strongly suggesting a near-orthogonal orientation of rotational and dipole axis. The main pulse profile exhibits asymmetry which looks consistent with the implications of eqs. (7) and (8): the components on the leading side are very broad and strongly merged with each other, whereas the components on the trailing side, despite being located much closer to each other, can still be identified through the noticeable minima between them. The trailing components must then be much narrower than the leading ones. Because of the blending the exact width of the components cannot be determined. However, because the components are nevertheless identifiable, we assume that their widths are similar to the components’ separation.

For the leadingmost component of the MP we use the width of $\Delta\phi_L \simeq -15^\circ$ which is marked by the leftmost pair of vertical solid lines in Fig. 6. The width can be used to estimate the corresponding range of radial distance Δr . From eq. (7) we have:

$$\frac{r_2}{R_{\text{lc}}} \simeq \left(\sqrt{\frac{9}{64}s^2 - \frac{1}{2} \left[\Delta\phi_L - \frac{3}{2}s \sqrt{\frac{r_1}{R_{\text{lc}}}} - 2\frac{r_1}{R_{\text{lc}}} \right] - \frac{3}{8}s} \right)^2. \quad (28)$$

For $r_1 = 10^6$ cm and $s = 1$ we get $r_2 \simeq 2.3 \cdot 10^6$ and $\Delta r = r_2 - r_1 \simeq 1.3 \cdot 10^6$ cm. Thus, the width of components on the leading side of the MP implies the radial extent of the order of the NS radius R_{NS} .

Assuming approximate symmetry of the outer cone with respect to the $(\Omega, \vec{\mu})$ -plane in the CF, one can use the derived value of Δr in eq. (8) to estimate the width of the components on the TS of the MP and thereby to test the reasoning. For $r_1 = 10^6$ cm and $r_2 = 2.3 \cdot 10^6$ cm eq. (8) gives $\Delta\phi_T \simeq 2.9^\circ$, which is marked in Fig. 6 by the pair of the vertical solid lines on the right-hand side. The width-scale of the leading and trailing components is then consistent with the radio emitter's radial extent of the order of $\sim 10^6$ cm.

6.2 Component heights

However, the interpretation shown in Fig. 6 cannot be made consistent with the symmetry properties of ρ_{iof} . According to eq. (24), the IOF radius of curvature is symmetrical with respect to the caustic phase. Thus, both the caustic effects and ρ_{iof} -driven emissivity should be symmetrical with respect to ϕ_{cst} . For $r < 0.14R_{\text{lc}}$ the caustic phase always precedes the trailingmost component (if the latter is assumed to have $s = 1$). The height of components, ie. the flux $F(\phi)$, is then expected to fall off symmetrically on both sides of some phase located within the pulse window. In the main pulse of J1012+5307 the flux increases monotonically towards its extreme trailing edge which can be interpreted in two ways: 1) the profile is shaped by physical effects independent of ρ_{iof} ; 2) the emission region is not centered at the dipole axis, but is located fully on the LS of the caustic coordinates.

In the second case, ϕ_{cst} needs to be located somewhere on the right-hand side of the trailingmost component. Since no observed features can be noticed there, and the available model parameters allow for some fit ambiguity, in Fig. 7 we present just a sample profile calculated for ϕ_{cst} located at the phase of the trailingmost component. The modelled profile (bottom solid line) has been obtained for $r_1 = 10^6$, $r_2 = 2 \cdot 10^6$ cm, $\Delta s = 0.1$, $\alpha = \zeta = 90^\circ$ and for uniform emissivity per centimeter of IOF trajectory. The component on the extreme right-hand side is located right at the caustic phase $\phi_{\text{cst}} \simeq 7^\circ$ (for $r_{\text{av}} = 1.5 \cdot 10^6$ cm). Its width and height are therefore mostly determined by the magnitude of Δs . The flux on the LS is dominated by the effects of ρ_{iof} . In these two limits the flux is well approximated with the analytical model (27) (dashed line, symmetric around ϕ_{cst}). In the intermediate region [phase range $(-5^\circ, 5^\circ)$] the agreement is worse. The values of s parameter have been selected for each component to match the observed pulse phase and vary from $s = 1$ for the component on the leading edge, through $s = 0$ near the central minimum, to the caustic value of $s = 0.6$ for the trailingmost component.

The numerical profile exhibits the general observed properties, ie. the monotonic increase of flux towards the TS and the narrower components on the TS. The LS/TS flux ratio could be made more consistent with data by placing ϕ_{cst} far on the trailing side. However, such fit would not be unique, because the ratio can also be adjusted by changing Δs and Δr . The difficulty in establishing ϕ_{cst} makes any multidimensional fitting procedure somewhat ambiguous and discourages us from forcing the model to closely match the data. The LS/TS asymmetry can also be probably decreased by increasing the impact angle $\beta = \zeta - \alpha$. Moreover, the observed profiles seem to be affected by the overlapping of neighbouring components. This cannot be easily modelled with our analytical formulae nor with the

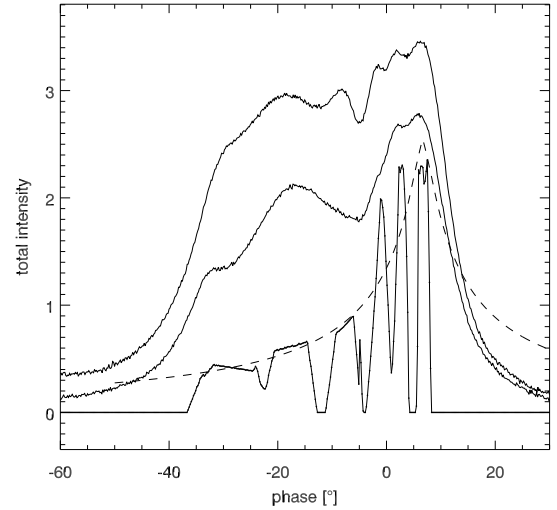


Figure 7. Numerically-calculated pulse shape (bottom curve) drawn below the J1012+5307 data. This uniform-emissivity model has $r_1 = 10^6$ cm, $r_2 = 2 \cdot 10^6$ cm, $\Delta s = 0.1$, and $\alpha = \zeta = 90^\circ$. Dashed curve presents eq. (27) with $a = 0$ and assumes that $\phi_{\text{cst}} = 7^\circ$.

numerical code, which creates pronounced spurious components caused by the sharp boundaries of the emission region at r_1 and r_2 . To avoid them, the code would have to be supplied with additional parameters that control the radial profile of emissivity.

The CR is physically better justified than the uniform emissivity model shown in Fig. 7, and it has been shown to produce enigmatic bifurcated components in the profile of J1012+5307 (Dyks, Rudak & Demorest 2009). In the case of the CR, a minimum of flux is expected at ϕ_{cst} . This suggests that the caustic phase be associated with the central minimum of the MP. We do not model this case, however, because the observed MP is not symmetric about this minimum (whereas the modelled profile would have been symmetric).

An alternative way to successfully model the profile is the cone-altitude approach of GG01, which assumes a set of the dipole-axis-centered rings of emission in the CF. Assuming that the near-surface emission within the main meridian is detected at the central minimum, the observed profiles can be reproduced if the rings are located at $s = 0.53, 0.7$, and 0.84 , and the average emission radius is equal to $1, 1.7$, and $2.5 \cdot 10^6$ cm, respectively.

Apart from J1012+5307, a similar systematic increase of flux towards the TS is exhibited by the central structure in the 438 MHz profile of J0437–4715 (Navarro et al. 1997).

7 CONCLUSIONS

We find that the shape of a profile is affected by two opposing effects of rotation: 1) the caustic enhancement of the TS, and 2) the increase of ρ_{iof} on the TS which decreases the centripetal acceleration and can thereby weaken the emissivity. The first can be viewed as a direct result of the straightening of an electron trajectory in the IOF, because the radiation

emitted within Δr is received within $\Delta\phi \simeq \Delta r/\rho_{\text{iof}}$. The radiation that constitutes the caustic peaks is emitted from the inflection points of IOF trajectories (or from regions of minimum IOF curvature in a non-orthogonal case). Formally, the caustic peaks are expected to occur at the phase of the center of the relativistically-shifted S-curve of the polarisation angle. The caustic phase, if calculated for the maximum $s = 1$, becomes the ‘maximum possible detection’ phase for tangent-to- \vec{B} radiation within the open region. Fast-rotating and highly-inclined pulsars are then expected to have pulse profiles with sharply defined (distinctively marked) trailing sides. On the LS, AR causes radiation from the outflowing electrons to be detected at a phase that monotonically increases with the emission altitude. The LS of the profile is thus expected to grow only gradually, creating a leading wing (the extent of which in practice is likely determined by the cooling timescale of the electrons).

Whether the leading or trailing side of the profile is the more enhanced by rotation is likely to be determined by the intrinsic dependence of the coherent emission mechanism on ρ_{iof} . In the case of the CR the emissivity is entirely driven by the macroscopic centripetal acceleration and we may expect a minimum in the zero curvature region. Otherwise, a caustic peak will dominate the profile (cf. Fig. 1b with 4c). Statistical analysis of millisecond profiles, could therefore provide limits on the possible value of the exponent a in the relation $F_{\text{coh}} \propto \rho_{\text{iof}}^a$. Inspection of published profiles suggests that $a \lesssim 0$ (as opposed to $a = -2/3$), although the number of good-quality millisecond profiles is very limited, and the interpretation of profiles in terms of a simple sum of emission components ignores possible absorption effects.

According to popular electrodynamic assumptions, the accelerating electric field is symmetrical with respect to the main meridian. However, the IOF curvature radii are intrinsically symmetric about the caustic phase at a given height (and asymmetric with respect to the dipole axis), so circular cones centered on this phase are theoretically likely. Because of the IOF-curvature asymmetry within the open region of fast rotating MSPs, the traditional, dipole-axis-centered nest of cones may be considered less natural than the decentered geometry of Fig. 5. In the extreme case of the fastest known MSPs ($P \sim 1.5$ ms), the caustic phase occurs at the outermost trailing edge of the polar cap, so it becomes difficult to generate a conal structure at all (possibly yielding the simplicity of the MP of B1937+21).

The main pulse of J1012+5307 exhibits asymmetry of flux and width which can be interpreted in terms of the corotational effects within a radially-extended emission region. The observed width of the main pulse suggests that the outermost components have $s \simeq 1$. This is roughly consistent with the widths of the outermost components if $r_1 \sim R_{\text{NS}}$ and $\Delta r \sim R_{\text{NS}}$. However, based solely on the symmetry of ρ_{iof} , the profile should then be symmetrical with respect to the caustic phase located somewhere within the main pulse window, which is not the case. This implies that either the profile is dominated by unknown ρ_{iof} -independent effects, or the emission region is located fully on the LS of the caustic coordinates. In the uniform-altitude scenario (same r_1 and r_2 for all components) this requires the rings/cones to be located asymmetrically with respect to the main meridian plane, but the location is not uniquely constrained because of the degeneracy of parameters. In the alternative cone-

altitude scenario, the asymmetry with respect to s_{cst} can still be achieved by a region that is symmetrical with respect to the main meridian in the CF. However, it is hard physically to justify the cone-altitude geometry. Neither of the scenarios is naturally consistent with the observed width of the main pulse, which is the same as the opening angle of the near-surface polar beam.

A possible solution to this problem is a model in which the polar tube at low altitudes is fully filled with the radio emission, and the minima observed in the MP result from absorption effects. The absorption could be provided by dense, opaque, radially-extended plasma columns in the polar tube. In this model the MP is not regarded as a sum of emission components. Rather, it is a single, box-like feature, with the minima of different width indented by the plasma columns. We expect that the minima will have essentially the same widths as the emission components in the emissive version of the model presented in Section 2. That is, the minima on the LS/TS will correspondingly be broad/narrow. Then, if the absorption occurred (on average) above $0.14R_{\text{lc}}$, it would be possible to avoid the problem of profile symmetry around ϕ_{cst} . Such an absorption-based scenario is supported by the box-like look of the MP of J1012+5307, and presents a promising subject for future study.

ACKNOWLEDGEMENTS

GAEW thanks the University of Sussex for a Visiting Research Fellowship. This paper was supported by the grant N203 387737 of the Ministry of Science and Higher Education.

REFERENCES

- Ahmadi P., Gangadhara R.T., 2002, ApJ, 566, 365
- Blaskiewicz M., Cordes J.M., Wasserman I., 1991, ApJ, 370, 643
- Buschauer R., Benford G., 1980, MNRAS, 190, 945
- Cheng K. S., Ruderman M. A., & Zhang L., 2000, ApJ, 537, 964
- Cordes J. M., 1975, ApJ, 195, 193
- Dyks J., 2008, MNRAS, 391, 859
- Dyks, J., & Rudak, B. 2002, A&A, 393, 511
- Dyks, J., & Rudak, B. 2003, ApJ, 598, 1201
- Dyks J., Harding A. K., & Rudak B., 2004, ApJ 606, 1125
- Dyks J., Rudak B., & Demorest P., 2009, MNRAS, in press (astro-ph/0908.1359)
- Gangadhara R. T., & Gupta Y., 2001, ApJ, 555, 31 (GG01)
- Kramer M., Xilouris K. M., Lorimer D., Doroshenko O., Jessner A., et al., 1998, ApJ, 501, 270
- Kramer M., Lange C., Lorimer D., Backer D.C., Xilouris K. M., et al., 1999, ApJ, 526, 957
- Krzyszowski K., Mitra D., Gupta Y., Kijak J., Gil J., & Acharyya A., 2009, MNRAS, 393, 1617
- Lommen A.N., Zepka A., Backer D.C., McLaughlin M., Cordes J.M., et al., 2000, ApJ, 545, 1007
- McConnell D., Ables J. G., Bailes M., Erickson W. C., 1996, MNRAS, 280, 331
- Morini M., 1983, MNRAS, 202, 495

Muslimov A. G., & Harding A.K., 2004, ApJ, 606, 1143
 370, 673
 Romani R.W., & Yadigaroglu I.-A., 1995, ApJ, 438, 314
 Słowikowska A., Kanbach G., Kramer M., & Stefanescu A.,
 2009, MNRAS, 397, 103
 Smith F. G., 1986, MNRAS, 219, 729
 Srostlik Z., Rankin J.M., 2006, MNRAS, xxx
 Stairs I.H., Thorsett S.E., Camilo F., 1999, ApJSS, 123,
 627 A&A, 445, 243 A&A, 469, 607

This paper has been typeset from a $\text{\TeX}/\text{\LaTeX}$ file prepared
 by the author.

APPENDIX A: EXTENSION OF THE MODEL TO NON-ORTHOGONAL PULSARS

For $\alpha \neq 90^\circ$ the rotationally-induced acceleration becomes $\vec{a}_\Omega \simeq 2\Omega c \sin \alpha \hat{e}_\phi$ (Dyks 2008) so that the IOF radius of curvature becomes

$$\rho_{\text{iof}} \simeq R_{\text{lc}} \left| \frac{3}{4} \frac{s}{\sqrt{r/R_{\text{lc}}}} \pm 2 \sin \alpha \right|^{-1}, \quad (\text{A1})$$

where the plus sign corresponds to the LS, whereas the minus is for the TS.

Near the star surface the equations hold with accuracy of $\sim 1\%$ (for $P \simeq 1$ s and α as small as 20°). For $P \simeq 5$ ms (and $\alpha = 20^\circ$) the accuracy is degraded down to typically $\sim 10\%$ and can be worse near the locations of zero curvature (cf. Fig. 3 for $\alpha = 90^\circ$).

If $\zeta \simeq \alpha$ it is also possible to extend the applicability of eqs. (2)-(8) to the non-orthogonal case of $\alpha \neq 90^\circ$. To do this the square root terms in eqs. (2)-(8) (but *not* the linear terms) need to be multiplied by $1/\sin \alpha$. This is because the ‘not a great circle effect’ expands the profile width while leaving the linear AR shift intact.

For example, the detection phase for the TS radiation becomes:

$$\phi_{\text{T}} \simeq \frac{3}{2} \frac{s}{\sin \alpha} \sqrt{\frac{r}{R_{\text{lc}}}} - 2 \frac{r}{R_{\text{lc}}} + \phi_f, \quad (\text{A2})$$

so that the caustic amplification determined by the condition $d\phi_{\text{T}}/dr = 0$ occurs for radiation emitted from:

$$\frac{r}{R_{\text{lc}}} \simeq \frac{9}{64} \frac{s^2}{\sin^2 \alpha}. \quad (\text{A3})$$

Thus, for a given r the caustic effects occur more in the central parts of the profile (smaller s) than in the orthogonal case, whereas for fixed s the caustic enhancement occurs at larger r . The amplification is observed at the phase:

$$\phi_{\text{cst}} \equiv \phi_{\text{max}} \simeq \frac{9}{32} \frac{s^2}{\sin^2 \alpha} + \phi_f = 16^\circ.11 \frac{s^2}{\sin^2 \alpha} + \phi_f, \quad (\text{A4})$$

ie. the caustic peaks occur further behind the MP than in the orthogonal case.

Though not related to the LS/TS asymmetry, it is also easy to find the IOF radius of curvature in the main meridian plane, where $\hat{\rho}_B \perp \hat{e}_\phi$. Using eqs. (19), (20), and the Pythagorean theorem we get

$$\rho_{\text{iof}} \simeq R_{\text{lc}} \left(\frac{9}{16} \frac{s^2}{r/R_{\text{lc}}} + 4 \sin^2 \alpha \right)^{-1/2}. \quad (\text{A5})$$